Thermal Structure of an Aluminum-Methane/air Hybrid Flame

Samuel Jeanjean, Justin Bertsch, Guillaume Legros, Christian Chauveau, Fabien Halter

THERMAL STRUCTURE OF AN ALUMINUM-METHANE/air HYBRID FLAME

Samuel Jeanjean*, Justin Bertsch, Guillaume Legros**, Christian Chauveau*, Fabien Halter***

Corresponding author. E-mail address: samuel.jeanjean@cnrs-orleans.fr (S.Jeanjean)

* CNRS – ICARE, 45071 Orléans, France

** Université d'Orléans, 45100 Orléans, France

Abstract

The modification of our energetic mix is one of the crucial challenges to mitigate climate change. Various solutions are studied, and we will probably use most of them in the future. One of these solutions is metal combustion. Indeed, metals have important energy properties, and the combustion of metal powder does not produce greenhouse gases except NOx, and also generates oxides which can be extracted then recycled to transform them back into fresh combustibles. Among others, Aluminum (Al) is very present on earth to gratify the potential global needs. As a matter of fact, Al possesses an important energetic density as compared to other metals like iron. Due to the difficulty of stabilizing dust flames only fed by Al in air, some applications should choose hybrid flames. The main objective of this study is to better characterize flames burning aluminum blended with CH_4. As an original contribution, a non-invasive methodology, i.e. two-color pyrometry, has been set up to do so. This article unveils the structure of such a flame fed by a high level of particle density. Through the observation of flame radiation and the evaluation of flame thickness, it was concluded that the quantity of injected methane could significantly change the regime of the central premixed flame that directly impacts the contribution of the diffusion flame to the reaction.

Keywords: Aluminum; Dust flame; Two-color pyrometry; Flame regime; Hybrid flame

1. Introduction

The scientific community agrees that human activity is significantly responsible for climate change and global warming by continuously increasing its consumption of fossil carbonaceous fuels. A decarbonization of our energy sources is mandatory [1]. A major issue in the development of alternative solutions to fossil fuels relies on our current incapacity to efficiently store energy. In this context, the development of carbon-free energy carriers is essential. The use of metallic particles as energy vectors may be a part of the solution. Metal powders could be envisaged storing and convey the energy [2]. The high energy density inherent to reactive metals, which motivates their use as additives to propellants and energetic materials, or as anodes within batteries, also inspires their use as recyclable solar fuels. In a concept of metal-fuel economy, metals, typically as powders, are burnt with air to produce heat for a heat engine. Metal fuels produce metal oxides, which are typically solid under standard conditions and can be collected for recycling. Metal fuels can be recycled from the metal oxide products, using clean primary energy sources, an effectively infinite number of times while avoiding loss of material to the environment. The proposed energy carrier would thus be used in a closed loop without generating greenhouse gases over its entire cycle [3]. Among all metals identified as possible energy carriers, silicon, aluminum, iron, and magnesium are the 2nd, 3rd, 4th, and 6th most abundant elements in the Earth's crust, respectively. The most abundant element being oxygen, typically in the form of an oxide of these metals. Iron is, by far, the most used metal today and is already envisaged as an energetic material [4, 5]. Aluminum has also been considered as a promising candidate

with interesting properties. Indeed, it has a specific energy of 31 MJ/kg, a quantity of raw material sufficient to meet global needs and the existence of an already developed recycling industry of its associated oxides (i.e. alumina Al_2O_3) [6]. That being said, the fundamental properties of Al/air two-phase flames are still poorly known as compared to traditional hydrocarbon flames [7].

An important part of the studies on metal combustion was undergone for large individual particles [8-11], more specifically for propellant and explosives applications. The study of stabilized flame has taken on particular importance over the last decades, especially under the impetus of the McGill group [12]. The establishment of a homogeneous gas / solid particle flow, its ignition, and the flame stabilization are extremely challenging. To the authors' knowledge, few groups are currently devoting efforts on it. Actually, it is highly difficult to obtain a stable combustion at long time scales fed by micrometric solid particles.

Particle dispersion has especially a major effect on the flame dynamics. Stretch and radiation effects also play an important role in the stabilization process, but their effects are still poorly understood. An original paradigm to enable both the use and characterization of these metal flames lies in the addition of a gaseous fuel. The combustion of a hybrid $CH_4/Al/O_2$ flame was recently studied by Palečka et al. [13-17]. These kinds of flames can also be encountered with metalized slurry fuels [18] or in the synthesis of nanoscale oxide [19] where metal particles are burnt in the combustion products of various hydrocarbon flames. A synthesis of metal combustion included hybrid combustion was made by Goroshin [20].

The current study aims at characterizing various hybrid $CH_4/Al/O_2$ flames for different methane contents. In particular, the flame structure is probed using a two-color pyrometry methodology.

2. Experimental setup and methodology

The flame is stabilized at the exit of a Bunsen type burner. A similar burner was already used by Lomba et al. [21]. A down-scale homothetic burner was built to facilitate stabilization of a laminar flame and to limit the quantity of oxide particles to filter in the exhaust. The burner has been designed to obtain a homogeneous and stable particle concentration at the burner outlet. It makes use of the principle of the previous burner (see Ref. [21] for more details) with an exit diameter of 20 mm in the present case. An annular (r_{int}=21.5mm r_{ext}=23.75mm) CH_4/Air pilot flame helps in the flame stabilization (see the green arrows in Fig. 1) This pilot flame emits less than 1% of the total power and so is negligible with respect to the main flame. The dispersion system was adapted from an industrial solid particle generator (LAVISION Particle Blaster 110) initially dedicated to PIV applications. This high-pressure fluidized bed generator has been modified to improve the aerosol generation. A flow of pure nitrogen (>99,99%) enters the system and is distributed by means of a torus perforated with calibrated holes (see the red arrows in Fig. 1). A magnetic stirrer located inside the disperser helps ensure constant concentration dispersion. The concentration exiting the system (see the black arrows in Fig. 1) was calibrated according to the quantity of particles introduced and the nitrogen flow rate. The nitrogen flow seeded with Al particles is then conveyed to the burner through an anti-static pipe. Oxygen and methane are directly connected to the bottom of the burner at a 4-injection head, and their flow rates were controlled by Bronkhorst mass flow controllers. The length of the burner and its divergent shape is sufficient to ensure a perfect mixing.

The duration of the steady state obtained for every experiment conducted was doubled thanks to the bunrer improvements. As an illustration, this leads to a 30-minute-long dispersion with 7.5 µm-mean-diameter particles. These changes also allow for an enhancement of the control of the flow rates. By modifying the system, the safety protocol

was also upgraded. The main air inlet was split into O_2 and N_2 inlets, that made dispersion possible only with nitrogen to avoid silo explosion.

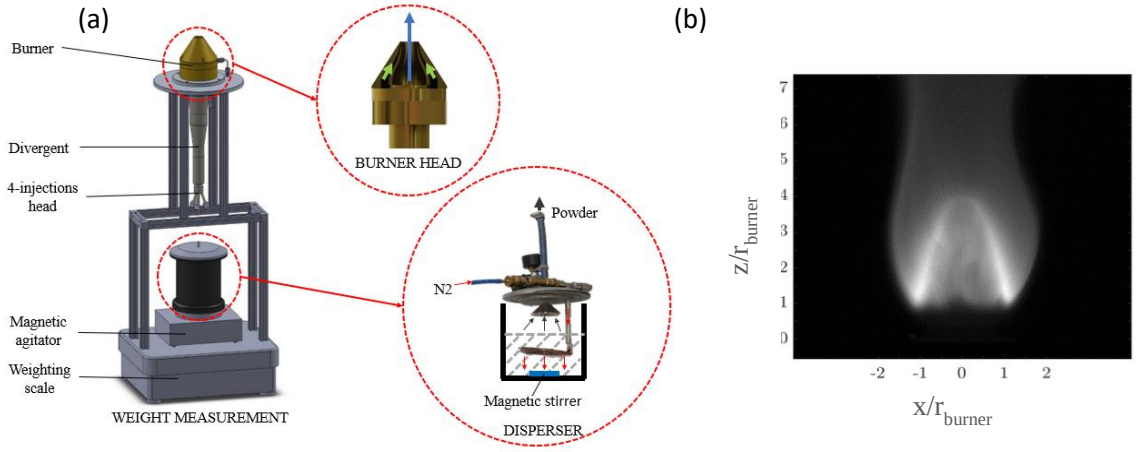

Figure 1. (a) Schematic of the burner and the disperser on the weighing scale. The green arrows represent the CH_4/air coflow and the blue arrow the CH_4/Al/air mixture.
(b) Instantaneous raw image of the flame with the 905 nm filter for a φ_{gazCH4} of 0.667

As illustrated in Fig. 1, both the burner and the disperser stand on a weighing scale. The scale can measure the accurate time evolution of the weight of the full system. The loss of mass corresponds exactly to the quantity of particles blown away to the burner. In previous our study [21], only the mass of the particles exiting the disperser was recorded without accounting for the deposit on the wall. A photodiode and a 670 nm laser (see (e) and (a) in Fig. 2 respectively) are used to double-check the density of the dispersed particles in the burner inflow [21]. The concentration is estimated by laser attenuation using the Beer-Lambert's method, where the spectral extinction coefficient was determined experimentally in non-reactive tests. The weighing scale provides global information whereas the photodiode/laser system provides local information; it checks the particle density only along the beam. This double-check allows having a perfect idea of the total amount of dispersed particle and to know if it is spatially well distributed. In future work, a fluxmeter will be used to assess the flame radiation in order to quantify energy balance. A spectrometer OceanOptics FX-XR1 was also used.

The optical setup assembled around the burner (see Fig. 2) allows two-dimensional fields of combustion condensed products temperatures to be measured. To do so, two cameras (PCO.edge 5.5) are located behind a beam splitter (h) to capture either the transmitted image of the flame (camera (j)) or the reflected one (camera (l)). The optical path from the burner (b) to each camera is the same. The two cameras are equipped with identical lenses (Nikon AF MICRO NIKKOR 105 mm 1:1.8 D). Each camera is equipped with a bandpass filter, i.e. (k) one centered at 700 nm (FWHM = 10 nm) and (i) one centered at 905 nm (FWHM = 10 nm). Both spectral ranges were selected to stand both within the range of the camera sensor and away from the AlO, Al(g), and CH* emissions bands. In addition, forecasting the condensed phase temperature (around 3200K [21]) and considering the particles as gray body, the spectral range around 900 nm is expected to be close to the captured emission. A black surface (g) is located on another side of the beam splitter to reduce the effect of the background contribution to the signals captured. A signal generator (c) controls both cameras simultaneously, triggering simultaneous onset of the imaging and setting the same exposure time.

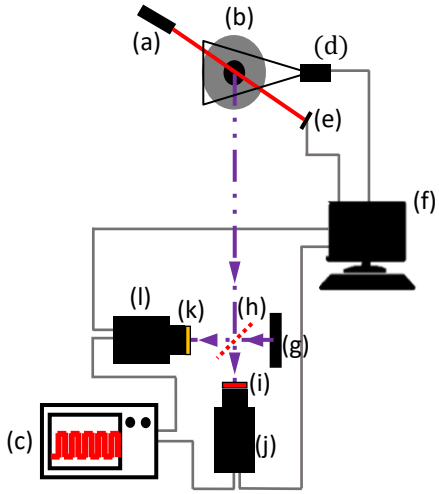

Figure 2. Experimental Optical Setup (a) 670 nm diode laser (b) burner (c) oscilloscope (d) fluxmeter (e) photodiode (f) computer (g) black surface (h) beam splitter (i) 905 nm filter mounted on the lens (k) 700 nm filter mounted on the lens (j) first camera (l) second camera.

To overlay the simultaneous capture of 2 frames, a test pattern (White Single-sided QR-Code Calibration Plate from LaVision) located above the burner is imaged before each experiment. This pattern allows correcting for any possible image distortion [22][2]. Four points are used to apply a projective adjustment, i.e. the correction converges translation, rotation, scaling, parallel lines toward a vanishing point. It is believed that the optical bench does not bend the picture as straight lines remain straight. An intensity correction also has to be considered. Different bandpass filters are used (700 and 905 nm) due to their different transmission properties, and the camera sensor response is specific to a given spectral range. The linearity of the pixels response was checked imaging a flat light CCS TH2-160/120-SW-PM powered by a PD3-5024-4EI(A). A tungsten filament was also used to determine the correction coefficient to be applied to each camera (l and j). To consider only a section of the flame, a deconvolution with an Abel reverse transformation was applied on each image using the Basex method [23]. The used image can be deconvoluted because the flame is axisymmetric. Moreover, we will consider particles as gray bodies in studied wavelengths because the emissivity decreases with wavelengths in $1/\lambda$ [24] and the studied wavelength are high, so the emissivity stay close. The two near-IR-range selected wavelengths are close enough to justify our gray body hypothesis.

To compute the temperature (T), the local spectral intensity $L(T,\lambda)$ is considered to be governed by Planck's law [25] weighted by the emissivity ε(λ) where λ is the wavelength:

$$L(T,\lambda) = \frac{\varepsilon(\lambda) 2h\pi c^2}{\lambda^5 \left(e^{\frac{hc}{\lambda k T}} - 1\right)} \quad (1)$$

with $k = 1.3807\ 10^{-23}\ J/K$ being the Boltzmann constant, $h = 6.626\ 10^{-34}\ J.s$ the Planck constant, and c the speed of light in the medium, which can be considered as that in a vacuum ($2.998\ 10^{8}\ m/s$) in the present study.

By considering the particles as gray bodies (ε(λ)=const.), and by computing the ratio of local spectral intensities, another simplified equation is considered:

$$\frac{L_1}{L_2} = \left(\frac{\lambda_2}{\lambda_1}\right)^5 \frac{e^{\frac{hc}{\lambda_2 kT}} - 1}{e^{\frac{hc}{\lambda_1 kT}} - 1} \quad (2)$$

with L_1 and L_2 the local spectral intensities at wavelength λ_1 and λ_2, respectively. This equation expresses the ratio of Planck's law at two different spectral ranges. The two ranges are fixed, the local spectral intensity is measured, and the emissivity of the condensed particles is taken as constant for these two close spectral ranges. The only unknown factor is the temperature.

This process allows providing a 2D field of the condensed phase temperature. A similar experiment done by S. Goroshin [26] allows providing a 1D temperature field. In a following research done by M. Soo [27], the methodology used by S. Goroshin was criticized. The main problem was that an assumption of low optical thickness was used for a flame with high optical thickness. For this reason, we will not consider the flame temperature value here, but the temperature trend.

The ignition sequence consists of starting first the pilot flame and then the main flame supplied by a stoichiometric CH_4/Air mixture. Then Al particles are injected into the system and the CH_4 flow is progressively reduced to its targeted value. For a matter of legibility, an equivalence ratio only based on the CH_4/Air mixture will be introduced to describe the quantity of the methane content, without considering aluminum. This quantity will be referred to as φ_{gasCH4}. Five different methane contents were considered. These different methane concentrations lead to five CH_4-lean equivalence ratios ranging between 0.4 and 0.9. For all conditions, the Al concentration is kept constant at 560 g/cm^3.

3. Results and discussions

3.1 Flame luminosity

A first observation of the luminance emitted by the different flames is performed based on the average intensity field imaged within both selected spectral ranges, i.e. 700 and 905 nm. Any instantaneous flame image such as that displayed in Fig. 1(b) exhibits a brighter zone forming a central conical shape. This intensity is highly dominated by the hot condensed particles' emission. As particles may be considered as gray bodies, the collected intensity depends on both their temperature and concentration. For each methane content, 200 images were averaged keeping constant camera settings (exposure time, aperture, neutral density filter). Averaging takes account of the flame flickering induced by the dispersion process. In fact, some agglomerates can be transported by the flow, leading to locally brighter zones. The maximum intensity of each CH_4 content was then normalized by the brightest condition. Its evolution as a function of the methane content is presented in Fig. 3. The evolution of the maximum intensity is probably due to a drop of the temperature when raising the CH_4 concentration. Indeed, increasing the CH_4 content, aluminum particles experience lower oxidizing conditions to react. It is admitted that CH_4 burns in priority. So in general, the methane reaction zone is upstream of the particles one as the latter need to be heated up to reach the aluminum vaporization temperature and to fragment the oxide layer [15, 17]. Performing spectroscopy on the different flames confirms that the CH* emission is by far lower than the condensed particles emission. Moreover, AlO radical radiates also more than the CH* radical while both emit within similar spectral ranges (AlO emits from 420 to 540 nm and CH* does so from 390 to 500 nm). As a consequence, it was impossible to clearly identified the CH* radical production location to confirm that methane reacts prior to metal particles.

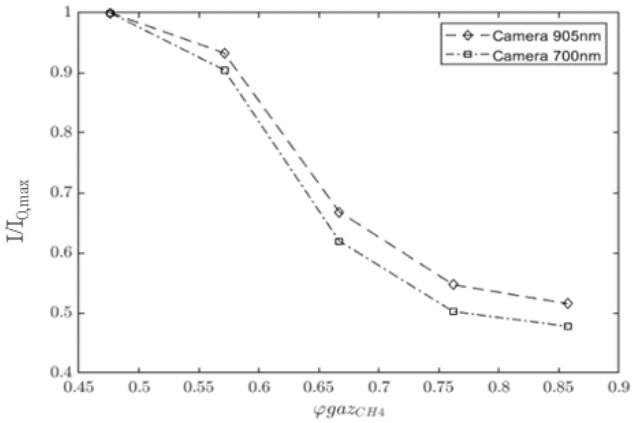

Figure 3. Evolution of the maximum intensity of average images on both cameras as a function of the equivalence ratio based on the methane content.

The maximum intensity variation is clearly not linear with the equivalence ratio and presents a change of behavior for leaner and richer conditions. This point will be discussed and explained later on.

3.2 Study of the flame structure

To account for the axisymmetric geometry of the configuration, flame images are deconvoluted. Half a deconvoluted flame image (φ_{gasCH4}=0.857) is presented in Fig. 4. It is worth reminding that for all methane contents, Al concentration was kept constant at 560 g/cm^3 (the stoichiometric fuel concentration in aluminum/air suspension is about 305 g/cm^3). With these conditions, CH_4 rapidly consumes most of the oxygen. On Fig. 4, only the right half of the flame is displayed, knowing that the burner exit is located from 0 to 1. A typical double-flame structure is observed, i.e. a conical premixed flame for x/r ranging from 0 to 1 (where r is the burner radius) and a diffusion flame on the outer side (for x/r ranging from 1 to 2)). A red dashed line has been added to schematically delineate the limit between both flames. The image can be used to identify the most radiant zones (here done at 905 nm). Unlike what was done for the brightness of the flame, the camera settings are optimized to use the whole sensor dynamic. The exposure time was adjusted just before

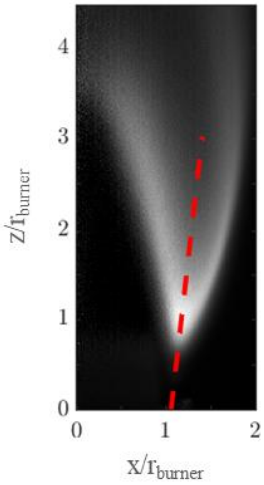

Figure 4. Right half of a flame image after deconvolution process. The red dashed line schematically delineates the limit between the premixed (left-hand side) and the diffusion (right-hand side) flames. All the axes are normalized with the radius of the burner.

reaching the saturation. The few overexposed images were not considered for averaging. To account for the flame volume, the intensity at location (x/r) is weighted by x/r. This procedure allows considering the integrated flame. The obtained quantity is abusively called radiative intensity. Lines of iso-level set at 20% of the maximum local radiative intensity are reported in Fig. 5(a) for the 5 methane contents. It allows the evolution of the double flame to be tracked without considering the plume contribution. Once more, a dashed line schematically delineating the limit between the premixed (left-hand side) and the diffusion (right-hand side) flames is drawn. It was admitted that a linear line was enough to separate the two flames knowing that the real limit is a mix between diffusion and premixed flame zone. To quantify the contribution of the premixed flame to the global emission, the ratio between the integrated radiative intensity attributed to the premixed flame to that of the whole flame is evaluated (Fig. 5(b)). This ratio highlights the fact that the higher CH_4 flow rate, the more important the diffusion flame.

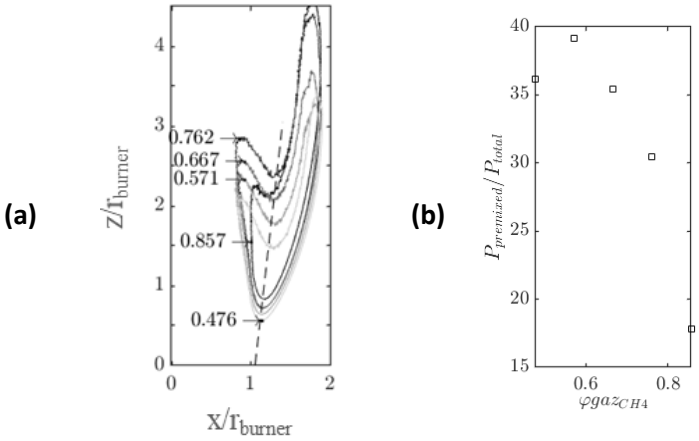

Figure 5. (b) Lines of iso-level set at 20% of the maximum local radiative intensity. These are identified on average images captured at 905 nm. The different CH_4 equivalence ratios are reported on each individual line. The dash line schematically delineates the limit between the premixed and the diffusion flames.
(b) Evolution of the ratio between the integrated radiative intensity attributed to the premixed flame to that of the whole flame.

By increasing the methane content, the premixed flame is less powerful because less aluminum can burn in this zone due to the lack of oxygen. However, more particles are available to burn into the outer diffusion flame with the ambient air. This explains the decrease in the radiative intensity of the premixed flame for the benefit of the diffusion flame. Note that the absolute radiative contribution of the diffusion flame also decreases when methane is added. A peculiar behavior is observed in the CH_4-leanest condition. This trend reversal can be explained by a change of regime. Above a certain amount of CH_4, methane burns upstream the aluminum and then allows a preheating of Al particles, that should correspond to a control (two separate flame fronts) and merged (only one flame front) modes [28]. According to the measurement given by the fluxmeter (Figure 2), it can be concluded that the aluminum radiation intensity is about ten times brighter than CH4. Even by isolating CH* emission (400-480nm), the gray body contribution is still too important. The CH4 flame cannot be directly observed, and so only hypothesis can be given: by adding CH_4, the preheating becomes more intense if we consider that methane consumes the available oxygen preferentially, but the rate of oxygen left for the aluminum oxidation is lower (the control mode). Below this critical amount, the CH_4 and aluminum reaction zone overlaps. Methane preheats the particles to a far lower extent, and consumes oxygen, which can correspond to a single flame front mode (the merge mode).

3.3 Flame Temperature

Temperature fields of the condensed phase are evaluated following Eq. (2) and using both sets of images. Half a field of temperature is presented in Fig. 6 for φ_{gazCH4}=0.67. The solid black line joins the locations of the maximum radiative intensity at every height (using the 905 nm image). A region of interest is defined so that all zones of low emission intensity are disregarded. Due to the process, the removed zone is noisy and unusable. Note that a band in the middle is also removed, the deconvolution provides disturbance at this place. In doing so, only the regions of higher temperature are mapped.

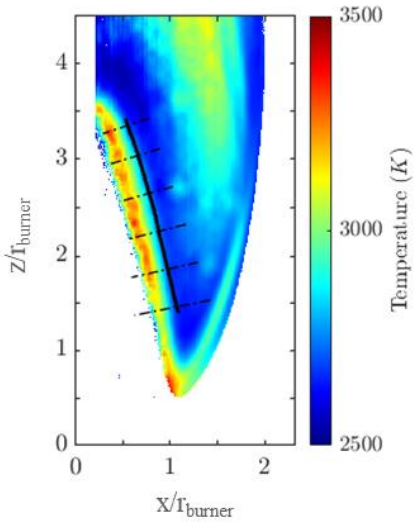

Figure 6. Half field of temperature for a φ_{gazCH4} of 0.667. The solid black line joins the locations of the maximum radiative intensity at every height. These are identified on average images captured at 905 nm. The dashed lines display a set of normals to the solid black line.

This line does not clearly follow the locations of the maximum temperature. As already mentioned, the emitted intensity depends on both the temperature and the particle concentration. This means that the alumina particles nucleation and growth take a certain time after the gas-phase reaction burnout. Although the condensation is an exothermal process, the temperature is decreasing when particles move downstream the conical premixed reaction zone. This is likely to be due to radiation heat losses. Particles density and size are more important at the location of the maximum density than in the high temperature zone. This high temperature zone exhibits values around 3200 K which is consistent with the gas-phase combustion temperature of Al particles in air. With this methane content (φ_{gazCH4}=0.667), a large quantity of evaporated aluminum condenses back without being oxidized. Comparing the relatively high level of temperature encountered in the burnt zone to the aluminum boiling temperature (2790K at 1 atm), part of the aluminum may remain gaseous. Aluminum that certainly condenses forms small particles that can easily burn. The gaseous aluminum emits below 400 nm, so its emission is not captured by the camera (and is weak in comparison with the condensed particles' emission). When the oxidizer is fully consumed, the particles temperature drops due to radiation and convection. Considering the temperature evolution along a normal to the black line (maximum radiative intensity), a temperature drop to 2700 / 2800 K is observed prior to a slight increase (yellow zone on the top of Figure). This increase that corresponds to the plume will be discussed below. Despite uncertainties in the deconvolution and the quotient, the calculated temperatures seem to be consistent. Indeed, the reached temperature by the drop is close to the condensation bearing

of the aluminum which seems logical. However, these temperatures were given near the highest intensity value after deconvolution. The quotient provides more significant errors at low intensity level. As mentioned before, the high optical thickness does not allow us to confirm this temperature. In the continuation of the study, only the trend of the temperature will be discussed and not the absolute temperatures.

Fig. 6 also illustrates the presence of a diffusion flame on the outer flame zone (x/r between 1 and 2). The temperature in this zone is lower, probably due to a low local aluminum density. The aluminum particles are too distant from each other to capture enough energy by radiation which does not favor their ignition and combustion.

In the plume (at the top of Fig. 6), a temperature increase is clearly visible, reaching temperatures around 3000 K. Oxygen is provided by the external air. This air supply favors the combustion of the remaining aluminum (either gaseous or small re-condensed particles). This zone does not seem to have a clear boundary [29]. Three major explanations can be stated: i) aluminum is both gaseous and condensed into particles of varying sizes, all of them burning with different characteristic times; ii) gradients in oxygen concentration are important in this zone which also contains CO_2 and H_2O coming from the methane oxidation; iii) the flow speed is relatively important due to the local high temperature conditions so the residence time of the particles can be short as compared to the combustion time, especially in the presence of a medium highly diluted in carbon dioxide.

We have focused our analysis on one specific methane content but all the conditions exhibit a similar flame structure, with a more or less pronounced importance of the external diffusion flame. Thus, three flames are observed, namely a conical premixed flame, an external diffusion flame, and a reaction zone with no clear interface in the plume. However, some differences exist in the intern structure of the reaction zone as shown in the next part.

3.4 Flame Thickness

Temperature profiles (see the dashed black lines in Fig. 6) can be evaluated normal to the maximum radiative intensity line (solid black line in Fig. 6). These profiles were evaluated along the maximum radiative intensity line starting from the bottom (h/r ~ 1.5 to 3.5, with h as the height from the exit of the burner and r, the radius of the burner). Each profile exhibits a very similar evolution, i.e. there is a significant rise in temperature up to a maximum temperature T_1 (about 3200 K) (aluminum gas-phase reaction location), then a decrease to a minimum T_2 (about 2700 K), due to radiation heat losses, and finally a temperature increase in the plume. A characteristic flame thickness has been defined to describe the evolution of the width of the premixed flame zone. This thickness corresponds to the width of the temperature profile for $T_3= (T_1+T_2)/2$. This study was carried out on 200 profiles on each ten most symmetric individual images to avoid any filtering effect. This allows collecting more than 2000 values of thickness for each condition. Note that T_1 and T_2 are not constant because they depend on each image and the positions in these images.

The evolution of flame thickness along the normalized height is reported in Fig. 7. It is noticeable that the thickness is wider near the tip of the flame (h/r ~ 3.5) than at its base (h/r ~1.5). This thickening of the premixed reaction zone along the flame front has already been reported by Goroshin et al. [30]. This is related to curvature effects.

The thickness dispersion observed in Fig. 7 is mainly due to the flame flickering. To avoid being impacted by extreme value, the most probable thickness was evaluated. This information is documented in Fig. 8 as a function of the methane content. Dispersion has been determined considering the error on the overlaying of two images. This provides a shift of 3-pixels, which corresponds to 0.025 cm. Error bars have been added in Fig. 8. As previously noticed (see Fig. 5(b)), a change in behavior occurs for the lowest gas equivalence

ratio. The slop will not be studied due to a high noise compared to the evolution of the thickness.

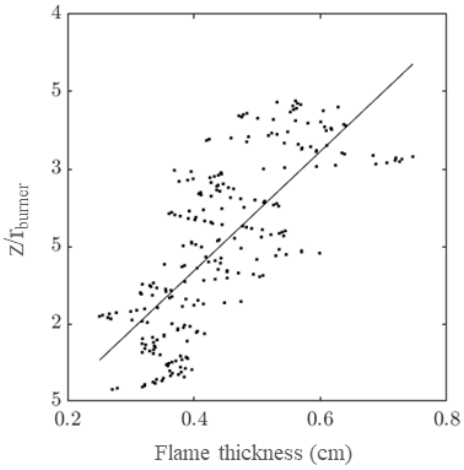

Figure 7. Evolution of the flame thickness along the height of the flame for $\varphi_{gazCH4} = 0.667$.

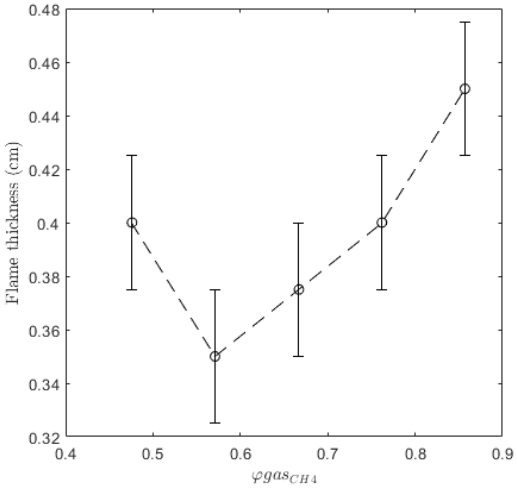

Figure 8. Evolution of the most probable flame thickness with φ_{gazCH4}.
The dispersion (error bar) is represented by the rms value of the population.

This trend reversal can be explained by a change in regime. Decreasing the methane content makes the CH_4/Air and Al/Air flame fronts closer to each other as the reactivity of both flames increases (i.e. methane/air flame speed decreases and conversely aluminum/air flame increases as the available oxygen increases). Palečka et al. [31] demonstrated that the premixed flame thickness decreases when the regime changes from the separated regime to the merged regime. Moreover, Braconnier et al. [32] observed that for an isolated particle, reactivity increase with the oxygen content in a O_2/CO_2 atmosphere. In the limit of a totally merged regime, the two flame fronts are superimposed. As a consequence, the methane/air flame does not significantly preheat the aluminum particles which slow down their ignition. This directly impacts the temperature thickness. The thickness increase occurs before the total merging of the two flame fronts. Reality is slightly different as particle size distributions are always large meaning that small particles continue to ignite in the vicinity of the methane/air flame whereas large particles ignite further away as was observed for binary suspension of solid fuel particles [28].

4. Conclusion

Hybrid Aluminum/Methane/Air flames have been stabilized on a laminar Bunsen-type burner. The methane content was varied to range from a strong methane-influenced flame to a slightly hybridized one. Direct visualizations of flame luminosity together with local temperature fields were jointly analyzed to document the flames' structure.

For all methane contents, the flame can be divided into 3 distinct reaction zones: i) a premixed flame where methane and part of the aluminum particles burn; ii) an external diffusion flame where the unconsumed aluminum reacts with ambient air; iii) a reaction zone located in the downstream plume in which unconsumed aluminum reacts with produced CO_2 /H_2O and air from the induced outer flow. When the methane consumes almost all the oxygen injected in the premixed flame, the aluminum reacts mainly within the external diffusion flame and/or in the plume.

The inner structure of the conical premixed flame depends on the methane content. For high methane contents, two successive reaction zones are observed: the first corresponding to the sudden oxidation of methane with oxygen and the second one to the oxidation of aluminum particles with the remaining oxygen. When the methane content is decreased, these two distinct zones merge into a unique one. This results from a competition between the increase of the amount of available oxygen for aluminum particles oxidation and the decrease of the energy released by methane oxidation.

A detailed study of the temperature evolution made it possible to confirm that the effects of curvature on the reactivity of the Al / Air flame are important.

In future works, we will examine the radiation and stretch effects on the stabilization of Al / air flames. It is important to continue a precise work on aluminum combustion.

5. Acknowledgements

The authors acknowledge the support of the French National Research Agency (ANR) under reference ANR- 18-CE05-0040.

6. References

[1] "IPCC, 2021: Summary for Policymakers. In: Climate Change 2021: The Physical Science Basis. Contribution of Working Group I to the Sixth Assessment Report of the Intergovernmental Panel on Climate Change," V. Masson-Delmotte, P. Zhai, A. Pirani, S. L. Connors, C. Péan, S. Berger, N. Caud, Y. Chen, L. Goldfarb, M. I. Gomis, M. Huang, K. Leitzell, E. Lonnoy, J.B.R. Matthews, T. K. Maycock, T. Waterfield, O. Yelekçi, R. Yu and B. Zhou, ed., Cambridge University Press. .

[2] Bergthorson, J. M., "Recyclable metal fuels for clean and compact zero-carbon power", *Prog. Energy Combust. Sci.* 68: 169-196 (2018).

[3] Julien, P., Bergthorson, J. M., "Enabling the metal fuel economy: green recycling of metal fuels", *Sustain. Energy Fuels* 1(3): 615-625 (2017).

[4] Ning, D., Shoshin, Y., van Oijen, J. A., Finotello, G., de Goey, L. P. H., "Burn time and combustion regime of laser-ignited single iron particle", *Combust. Flame* 230: 111424 (2021).

[5] Ning, D., Shoshin, Y., van Stiphout, M., van Oijen, J., Finotello, G., de Goey, P., "Temperature and phase transitions of laser-ignited single iron particle", *Combust. Flame* 236: 111801 (2022).

[6] Braaten, O., Kjekshus, A., Kvande, H., "The possible reduction of alumina to aluminum using hydrogen", *JOM* 52(2): 47-53 (2000).

[7] Trunov, M. A., Schoenitz, M., Dreizin, E. L., "Effect of polymorphic phase transformations in alumina layer on ignition of aluminium particles", *Combust. Theor. Model.* 10(4): 603-623 (2006).

[8] Friedman, R., Maček, A., "Ignition and combustion of aluminium particles in hot ambient gases", *Combust. Flame* 6: 9-19 (1962).

[9] Jackson, M., Pantoya, M. L., Gill, W., "Characterization of a gas burner to simulate a propellant flame and evaluate aluminum particle combustion", *Combust. Flame* 153(1-2): 58-70 (2008).

[10] Beckstead, M. W., "Correlating Aluminum Burning Times", *Combust. Explo. Shock Waves* 41(5): 533-546 (2005).

[11] Dreizin, E. L., "Experimental study of stages in aluminium particle combustion in air", *Combust. Flame* 105(4): 541-556 (1996).

[12] Julien, P., Vickery, J., Goroshin, S., Frost, D. L., Bergthorson, J. M., "Freely-propagating flames in aluminum dust clouds", *Combust. Flame* 162(11): 4241-4253 (2015).

[13] Julien, P., Soo, M., Goroshin, S., Frost, D. L., Bergthorson, J. M., Glumac, N., Zhang, F., "Combustion of Aluminum Suspensions in Hydrocarbon Flame Products", *J. Propul. Power* 30(4): 1047-1054 (2014).
[14] Soo, M., Julien, P., Goroshin, S., Bergthorson, J. M., Frost, D. L., "Stabilized flames in hybrid aluminum-methane/air mixtures", *Proc. Combust. Inst.* 34(2): 2213-2220 (2013).
[15] Palecka, J., Julien, P., Goroshin, S., Bergthorson, J. M., Frost, D. L., Higgins, A. J., "Quenching distance of flames in hybrid methane–aluminum mixtures", *Proc. Combust. Inst.* 35(2): 2463-2470 (2015).
[16] Palecka, J., Goroshin, S., Bergthorson, J. M., "Propagation and quenching of dual-front flames in binary-fuel mixtures", *Combust. Sci. Technol.* 190(9): 1557-1579 (2018).
[17] Palečka, J., Park, J., Goroshin, S., Bergthorson, J. M., "Aluminum-propane/air hybrid flames in a Hele-Shaw cell", *Proc. Combust. Inst.* 38(3): 4461-4468 (2021).
[18] Roy Choudhury, P., "Slurry fuels", *Prog. Energy Combust. Sci.* 18(5): 409-427 (1992).
[19] Zolotko, A. N., Vovchuk, Y. I., Poletayev, N. I., Florko, A. V., Al'tman, I. S., "Synthesis of nanooxides in two-phase laminar flames", *Combustion, Explosion, and Shock Waves* 32(3): 262-269 (1996).
[20] S. Goroshin, J. Palečka and J. M. Bergthorson, Some fundamental aspects of laminar flames in nonvolatile solid fuel suspensions, *Progress in Energy and Combustion Science* 91 (2022).
[21] Lomba, R., Laboureur, P., Dumand, C., Chauveau, C., Halter, F., "Determination of aluminum/air burning velocities using PIV and Laser sheet tomography", *Proc. Combust. Inst.* 37(3): 3143-3150 (2019).
[22] Reggeti, S. A., Agrawal, A. K., Bittle, J. A., "Two-color pyrometry system to eliminate optical errors for spatially resolved measurements in flames", *Appl. Opt.* 58(32): 8905 (2019).
[23] Dribinski, V., Ossadtchi, A., Mandelshtam, V. A., Reisler, H., "Reconstruction of Abel-transformable images: The Gaussian basis-set expansion Abel transform method", *Rev. Sci. Instrum.* 73(7): 2634-2642 (2002).
[24] Bohren, C. F., Huffman, D. R., Kam, Z., "Book-Review - Absorption and Scattering of Light by Small Particles", *Nature* 306: 625 (1983).
[25] M. Planck, On the Law of Distribution of Energy in the Normal Spectrum, *Annalen der Physik* 4 (1901).
[26] Goroshin, S., Mamen, J., Higgins, A., Bazyn, T., Glumac, N., Krier, H., "Emission spectroscopy of flame fronts in aluminum suspensions", *Proc. Combust. Inst.* 31(2): 2011-2019 (2007).
[27] Soo, M., Goroshin, S., Glumac, N., Kumashiro, K., Vickery, J., Frost, D. L., Bergthorson, J. M., "Emission and laser absorption spectroscopy of flat flames in aluminum suspensions", *Combust. Flame* 180: 230-238 (2017).
[28] Goroshin, S., Kolbe, M., Lee, J. H. S., "Flame speed in a binary suspension of solid fuel particles", *Proc. Combust. Inst.* 28(2): 2811-2817 (2000).
[29] Julien, P., Whiteley, S., Goroshin, S., Soo, M. J., Frost, D. L., Bergthorson, J. M., "Flame structure and particle-combustion regimes in premixed methane–iron–air suspensions", *Proc. Combust. Inst.* 35(2): 2431-2438 (2015).
[30] Goroshin, S., Fomenko, I., Lee, J. H. S., "Burning velocities in fuel-rich aluminum dust clouds", *Symp. (Int.) Combust.* 26(2): 1961-1967 (1996).
[31] Braconnier, A., Gallier, S., Halter, F., Chauveau, C., "Aluminum combustion in CO2-CO-N2 mixtures", *Proc. Combust. Inst.* 38(3): 4355-4363 (2021).